



ALMA as a Redshift Machine: Using [C II] to Efficiently Confirm Galaxies in the Epoch of Reionization

Sander Schouws¹, Rychard Bouwens¹, Renske Smit², Jacqueline Hodge¹, Mauro Stefanon¹, Joris Witstok^{3,4},
Juliëtte Hilhorst¹, Ivo Labbé⁵, Hiddo Algera⁶, Leindert Boogaard⁷, Michael Maseda⁸, Pascal Oesch^{9,10},
Huub Röttgering¹, and Paul van der Werf¹

¹ Leiden Observatory, Leiden University, NL-2300 RA Leiden, The Netherlands

² Astrophysics Research Institute, Liverpool John Moores University, 146 Brownlow Hill, Liverpool L3 5RF, UK

³ Kavli Institute for Cosmology, University of Cambridge, Madingley Road, Cambridge CB3 0HA, UK

⁴ Cavendish Laboratory, University of Cambridge, 19 JJ Thomson Avenue, Cambridge CB3 0HE, UK

⁵ Centre for Astrophysics and SuperComputing, Swinburne, University of Technology, Hawthorn, Victoria, 3122, Australia

⁶ Hiroshima Astrophysical Science Center, Hiroshima University, 1-3-1 Kagamiyama, Higashi-Hiroshima, Hiroshima 739-8526, Japan

⁷ Max Planck Institute for Astronomy, Königstuhl 17, D-69117 Heidelberg, Germany

⁸ Department of Astronomy, University of Wisconsin-Madison, 475 N. Charter Street, Madison, WI 53706 USA

⁹ Département d'Astronomie, Université de Genève, 51 Ch. des Maillettes, CH-1290 Versoix, Switzerland

¹⁰ International Associate, Cosmic Dawn Center (DAWN), Niels Bohr Institute, University of Copenhagen and DTU-Space, Technical University of Denmark, Denmark

Received 2022 February 7; revised 2023 June 5; accepted 2023 June 21; published 2023 August 25

Abstract

The [C II]_{158 μ m} line has long been proposed as a promising line to spectroscopically confirm galaxies in the epoch of reionization. In this paper, we present the results of new ALMA observations spectral scanning for [C II] in six particularly luminous Lyman-break galaxies at $z \sim 7$. The six sources were drawn from a sample of bright $z \sim 7$ galaxies identified using the wide-area optical, near-IR, and Spitzer/IRAC data over the COSMOS/UltraVISTA field and were targeted on the basis of tight constraints on their redshifts from their IRAC [3.6]–[4.5] colors. We detect significant ($>9\sigma$) [C II] lines in three of our six targets (50%) cospatial with the rest-UV emission from the ground/space-based near-IR imaging. The luminosities of the [C II] lines lie in the range $5.6\text{--}8.8 \times 10^8 L_\odot$, consistent with the local [C II]–SFR relation. Meanwhile, their [C II]/ $L_{\text{IR}} \sim 1\text{--}3 \times 10^{-3}$ ratios are slightly elevated compared to local (U)LIRGS. This could be due to lower dust-to-gas or dust-to-metal ratios. We also find that our sources display a large kinematic diversity, with one source showing signs of rotation, one source a likely major merger, and one dispersion-dominated source that might contain a bright star-forming clump. Our results highlight the effectiveness of spectral scans with ALMA in spectroscopically confirming luminous galaxies in the epoch of reionization, something that is being applied on a significantly larger sample in the ongoing REBELS large program.

Unified Astronomy Thesaurus concepts: Galaxy evolution (594); Galaxy formation (595); Galaxy kinematics (602); Lyman-break galaxies (979); Interstellar medium (847)

1. Introduction

Exploring the buildup of galaxies in the $z > 6.5$ universe just a few hundred million years after the Big Bang is a key frontier in extragalactic astronomy. Though hundreds of UV-bright galaxy candidates at redshifts $z > 6.5$ (e.g., McLure et al. 2013; Bouwens et al. 2015; Finkelstein et al. 2015; Ishigaki et al. 2018; Bouwens et al. 2021; Harikane et al. 2022) are known, characterization of their physical properties has been difficult. Deriving these properties from optical and near-IR photometry is complicated by uncertainties in the redshifts (e.g., Robertson 2022; Bouwens et al. 2022), dust extinction (e.g., Fudamoto et al. 2020; Bowler et al. 2022; Schouws et al. 2022), and rest-frame optical nebular emission-line properties (e.g., Smit et al. 2015; Endsley et al. 2021; Stefanon et al. 2022) of $z > 6$ galaxies.

Fortunately, with ALMA, it is possible to make great progress on the characterization of galaxies at $z > 6$ (e.g., Hodge & da Cunha 2020; Robertson 2022). The [C II]_{158 μ m}

line is especially interesting, as it is the strongest cooling line of warm gas ($T < 10^4$ K) in galaxies. This line has already been detected in a significant number of galaxies out to $z \sim 7\text{--}8$ (e.g., Walter et al. 2009; Wagg et al. 2010; Riechers et al. 2014; Capak et al. 2015; Willott et al. 2015; Knudsen et al. 2016; Pentericci et al. 2016; Bradač et al. 2017; Matthee et al. 2017; Carniani et al. 2018; Smit et al. 2018; Matthee et al. 2019; Béthermin et al. 2020; Carniani et al. 2020; Harikane et al. 2020; Le Fèvre et al. 2020; Venemans et al. 2020; Fudamoto et al. 2021). In addition to the immediate utility of [C II] to spectroscopically confirm galaxies in the reionization era and obtain a precise measurement of their redshift, the strength of this line makes it one of the prime features for studying the kinematics of high- z galaxies (e.g., Smit et al. 2018; Hashimoto et al. 2019; Jones et al. 2021). Dynamical masses are particularly interesting in that they give some handle on the masses of galaxies, which can be challenging to do from the photometry alone (e.g., Schaerer & de Barros 2009).

Despite the great utility of [C II] and the huge interest from the community, only a modest number of $z > 6.2$ galaxies had been found to show [C II] emission in the first six years of ALMA operations (e.g., Pentericci et al. 2016; Bradač et al. 2017; Matthee et al. 2017; Carniani et al. 2018, 2018;



Original content from this work may be used under the terms of the [Creative Commons Attribution 4.0 licence](https://creativecommons.org/licenses/by/4.0/). Any further distribution of this work must maintain attribution to the author(s) and the title of the work, journal citation and DOI.

Smit et al. 2018; Hashimoto et al. 2019). Additionally, even in cases where the [C II] line was detected, only modest luminosities were found, i.e., $L_{[\text{C II}]} \lesssim 2 \times 10^8 L_{\odot}$. One potentially important factor in the limited success of earlier probes for [C II] at $z > 6$ may have been the almost exclusive targeting of sources with redshifts from the Ly α emission line. At lower redshifts at least, Ly α emission seems to be much more prevalent in lower-mass galaxies than it is in higher-mass galaxies (e.g., Stark et al. 2010). Additionally, Ly α emitters have been found to be systematically low in their [C II] luminosity-to-SFR ratios (Harikane et al. 2018; Matthee et al. 2019). Both factors would have caused early ALMA observations to miss those galaxies with the brightest [C II] lines.

In a cycle 4 pilot, Smit et al. (2018) demonstrated the effectiveness of spectral scans for the [C II] line in $z > 6$ galaxies that are particularly luminous and also have well-constrained photometric redshifts. One aspect of the $z \sim 7$ galaxies from Smit et al. (2018) that allowed for particularly tight constraints on their redshifts was the high EWs of their strong [O III]+H β emission lines in the Spitzer/IRAC bands. This is due to the particular sensitivity of the Spitzer/IRAC [3.6]–[4.5] colors to redshift of galaxies for high-EW [O III]+H β emitters (Smit et al. 2015). Remarkably, despite just ~ 1 hr of observations becoming available on these targets, the results were nevertheless striking, with 6–8 σ [C II] lines found in two targeted sources, with redshifts $z = 6.8075$ and $z = 6.8540$. Additionally, the [C II] luminosities of the two sources were relatively high, being brighter in [C II] than all ALMA non-QSO targets by factors of ~ 2 –20.

Encouraged by the high efficiency of the Smit et al. (2018) spectral scan results, we successfully proposed for similar observations for six other luminous $z \sim 7$ galaxies (2018.1.00085.S; PI Schouws) to add to the results available from the Smit et al. (2018) program and further refine the spectral scan strategy. The purpose of this paper is to present results from this second pilot. Results from this pilot program and an earlier program from Smit et al. (2018) served as the motivation for the Reionization Era Bright Emission Line Survey (REBELS) ALMA large program (Bouwens et al. 2022) in cycle 7. The REBELS program significantly expanded the strategy employed in these pilot programs to a much larger set of targets, while extending the scan strategy to even higher redshift.

The paper is structured as follows. In Section 2, we detail the selection of targets for this second pilot program, while also describing the setup and reduction of our spectral scan observations. In Section 3, we describe the [C II] line search and present our new [C II] detections. We place our detections on the [C II]–SFR relation and examine the [C II]/ L_{IR} of our sources. We conclude the Section by examining their kinematics. In Section 4, we discuss the prospect of deploying the described spectral scan observations to a much larger set of $z > 6$ galaxies. Finally in Section 5, we summarize our conclusions.

Throughout this paper, we assume a standard cosmology with $H_0 = 70 \text{ km s}^{-1} \text{ Mpc}^{-1}$, $\Omega_m = 0.3$, and $\Omega_{\Lambda} = 0.7$. Magnitudes are presented in the AB system (Oke & Gunn 1983). For star formation rates and stellar masses, we adopt a Chabrier IMF (Chabrier 2003). Error bars indicate the 68% confidence interval unless specified otherwise.

2. High-redshift Targets and ALMA Observations

2.1. UltraVISTA Search Field and Photometry

Our source selection is based on ultra-deep near-infrared imaging over the COSMOS field (Scoville et al. 2007) from the third data release (DR3) of UltraVISTA (McCracken et al. 2012). UltraVISTA provides imaging covering 1.4 square degrees (McCracken et al. 2012) in the Y, J, H, and Ks filters to ~ 24 –25 mag (5σ), with DR3 achieving fainter limits over 0.7 square degrees in four ultra-deep strips. The DR3 contains all data taken between 2009 December and 2014 July and reaches $Y = 26.2$, $J = 26.0$, $H = 25.8$, $K = 25.5$ mag (5σ in $1''.2$ diameter apertures). The nominal depths we measure in the Y, J, H, and Ks bands for the UltraVISTA DR3 release are ~ 0.1 –0.2 mag, ~ 0.6 mag, ~ 0.8 mag, and ~ 0.2 mag, respectively, deeper than in the UltraVISTA DR2 release.

The optical data we use consists of CFHT/Omegacam in g, r, i, z (Erben et al. 2009) from the Canada–France–Hawaii Legacy Survey (CFHTLS) and Subaru/SuprimeCam in B $_r$ +V $_r$ +g+r+i+z imaging (Taniguchi et al. 2007). This analysis uses Spitzer/IRAC 3.6 μm and 4.5 μm observations from S-COSMOS (Sanders et al. 2007), the Spitzer Extended Deep Survey (SEDS; Ashby et al. 2013), the Spitzer-Cosmic Assembly Near-Infrared Deep Extragalactic Survey (S-CANDELS; Ashby et al. 2015), Spitzer Large Area Survey with Hyper-Suprime-Cam (SPLASH, PI: Peter Capak), and the Spitzer Matching survey of the UltraVISTA ultra-deep Stripes (SMUVS, PI: K. Caputi; Ashby et al. 2018). Compared to the original S-COSMOS IRAC data, SPLASH provides a large improvement in depth over nearly the whole UltraVISTA area, covering the central 1.2 square degree COSMOS field to 25.5 mag (AB) at 3.6 and 4.5 μm . SEDS and S-CANDELS cover smaller areas to even deeper limits. We also make use of data from SMUVS, which provides substantially deeper Spitzer/IRAC data over the deep UltraVISTA stripes.

Source catalogs were constructed using SExtractor v2.19.5 (Bertin & Arnouts 1996), run in dual-image mode, with source detection performed on the square root of a χ^2 image (Szalay et al. 1999) generated from the UltraVISTA YJHK $_s$ images. In creating our initial catalog of $z \sim 7$ candidate galaxies, we started from simply constructed catalogs derived from the ground-based observations. Prior to our photometric measurements, images were first convolved to the J-band point-spread function (PSF) and carefully registered against the detection image (mean rms $\sim 0''.05$). Color measurements were made in small apertures similar to those of Kron (1980) (SExtractor AUTO and Kron factor 1.2) with typical radii $\sim 0''.35$ – $0''.50$.

We also consider color measurements made in fixed $1''.2$ diameter apertures when refining our selection of $z \sim 7$ candidate galaxies. For the latter color measurements, flux from a source and its nearby neighbors ($12'' \times 12''$ region) is carefully modeled, and then flux from the neighbors is subtracted before the aperture photometry is performed. Our careful modeling of the light from neighboring sources improves the overall robustness of our final candidate list to source confusion. Total magnitudes are derived by correcting the fluxes measured in $1''.2$ diameter apertures for the light lying outside a $1''.2$ diameter aperture. The relevant correction factors are estimated on a source-by-source basis based on the spatial profile of each source and the relevant PSF-correction kernel. Photometry on the Spitzer/IRAC (Fazio et al. 2004) observations is more involved due to the much lower

resolution, $\text{FWHM} = 1''.7$, compared to the ground-based data ($\text{FWHM} = 0''.7$). The lower resolution results in source blending where light from foreground sources contaminates measurements of the sources of interest. These issues can largely be overcome by modeling and subtracting the contaminating light using the higher spatial resolution near-IR images as a prior. Measurements of the flux in the Spitzer/IRAC observations were performed with the *mophongo* software (Labbé et al. 2006, 2010a, 2010b, 2013, 2015). The positions and surface brightness distributions of the sources in the coadded JHKs image are assumed to be appropriate models, and after PSF matching to the IRAC observations, these models are simultaneously fit to the IRAC image, leaving only their normalization as a free parameter. Subsequently, light from all neighbors is subtracted, and flux densities were measured in $2''$ diameter circular apertures. The IRAC fluxes are corrected to total for missing light outside the aperture using the model profile for the individual sources. The procedure employed here is very similar to those of other studies (e.g., Galametz et al. 2013; Guo et al. 2013; Skelton et al. 2014; Stefanon et al. 2017; Weaver et al. 2022).

2.2. Bright $z \sim 7$ Selection

In effort to identify a robust set of $z \sim 7$ galaxies from the wide-area UltraVISTA data set for follow-up with ALMA, we require sources to be detected at $>6\sigma$, combining the flux in J , H , K_s , $[3.6]$, and $[4.5]$ band images (coadding the S/Ns in quadrature). The combined UltraVISTA + IRAC detection and S/N requirements exclude spurious sources due to noise, detector artifacts, and diffraction features. We construct a preliminary catalog of candidate $z \sim 7$ galaxies using those sources that show an apparent Lyman break due to absorption of UV photons by neutral hydrogen in the IGM blueward of the redshifted $\text{Ly}\alpha$ line. This break is measured using simple color criteria. At $z > 6.2$, the z -band flux is significantly impacted by this absorption of rest-UV photons, while at $z > 7.1$, the Y -band flux is impacted. The following criteria were applied:

$$(z - Y > 0.5) \wedge (Y - K < 0.7),$$

where \wedge is the logical AND operator. In case of a nondetection, the z or Y -band flux in these relations is replaced by the equivalent 1σ upper limit.

It is worth emphasizing that our final sample of $z > 6$ bright galaxies shows little dependence on the specific limits chosen here. For each candidate source, the redshift probability distribution $P(z)$ is then determined using the EAZY photometric redshift software (Brammer et al. 2008), which fits a linear combination of galaxy spectral templates to the observed spectral energy distribution (SED).

The template set used here is the standard EAZY v1.0 template set, augmented with templates from the Galaxy Evolutionary Synthesis Models (GALEV; Kotulla et al. 2009), which include nebular continuum and emission lines. The implementation of nebular lines follow the prescription of Anders & Fritze (2003), assuming $0.2 Z_\odot$ metallicity and a large rest-frame EW of $\text{H}\alpha = 1300 \text{ \AA}$. These extreme EW reproduce the observed $[3.6]$ – $[4.5]$ colors for many spectroscopically confirmed $z \sim 7$ – 9 galaxies (e.g., Ono et al. 2012; Finkelstein et al. 2013; Oesch et al. 2015; Zitrin et al. 2015; Roberts-Borsani et al. 2016; Stark et al. 2017). A flat prior on the redshift is assumed.

To maximize the robustness of candidates selected for our $z \sim 7$ samples, we require the integrated probability beyond $z = 6$ to be $>70\%$. The use of a redshift likelihood distribution $P(z)$ is very effective in rejecting faint low-redshift galaxies with a strong Balmer/4000 \AA break and fairly blue colors redward of the break.

The available optical observations are used to reject other low-redshift sources and Galactic stars by imposing $\chi_{\text{opt}}^2 < 4$. Here, χ_{opt}^2 is defined as $\chi_{\text{opt}}^2 = \sum_i \text{SGN}(f_i)(f_i/\sigma_i)^2$, where f_i is the flux in band i in a consistent aperture, σ_i is the uncertainty in this flux, and $\text{SGN}(f_i)$ is equal to 1 if $f_i > 0$ and -1 if $f_i < 0$. The value of χ_{opt}^2 is calculated in both $0''.8$ diameter apertures and in scaled elliptical apertures. χ_{opt}^2 is effective in excluding $z = 1$ – 3 low-redshift star-forming galaxies, where the Lyman-break color selection is satisfied by strong line emission contributing to one of the broad bands (e.g., Atek et al. 2011; van der Wel et al. 2011). Sources that show a 2σ detection in the available ground-based imaging bands (weighting the flux in the different bands according to the inverse square uncertainty in f_i) are also excluded as potentially corresponding to lower-redshift contaminants. Finally, to minimize contamination by low-mass stars, we fit the observed SEDs of candidate $z \sim 7$ galaxies both with EAZY and with stellar templates from the SpecX prism library (Burgasser et al. 2004). Sources that are significantly better fit ($\Delta\chi^2 > 1$) by stellar SED models are excluded. The SED templates for lower-mass stars are extended to $5 \mu\text{m}$ using the known J – $[3.6]$ or J – $[4.5]$ colors of these spectral types (Patten et al. 2006; Kirkpatrick et al. 2011) and the nominal spectral types of stars from the SpecX library. The approach we utilize is identical to the SED-fitting approach employed by Bouwens et al. (2015) for excluding low-mass stars from the CANDELS fields. Combined, these selection requirements result in very low expected contamination rates.

Using the above selection criteria, we select 32 $z \sim 7$ potential candidates for spectral scans over a 1.2 square degree area in the UltraVISTA field. The sources have an H -band magnitude ranging from 23.8 mag to 25.7 mag and redshifts 6.6 to 7.1. We include a list of the sources we select in Table 3 from the Appendix.

2.3. Target Selection for the ALMA Observations

In an effort to further demonstrate the potential of spectral scans with ALMA to characterize massive star-forming galaxies at $z \sim 7$, we elected to target six sources from the $z \sim 7$ galaxy sample constructed in the previous section (and which is presented in the Appendix).

We focused on those galaxies that are brightest in the rest-frame UV and have the tightest constraints on their photometric redshifts. UV-bright galaxies are particularly useful to target because those sources have the highest apparent SFRs and should contain particularly luminous $[\text{C II}]$ lines, assuming the De Looze et al. (2014) relation holds out to $z > 6$ as Schaerer et al. (2020) find. If there is an additional contribution from obscured star formation, the luminosity of $[\text{C II}]$ should be further enhanced.

Additionally, it is useful to target sources with tight constraints on their redshifts from photometry to minimize the number of spectral scan windows that need to be utilized. For this purpose, a useful set of sources to target are those with particularly strong constraints on their photometric redshifts from their Spitzer/IRAC

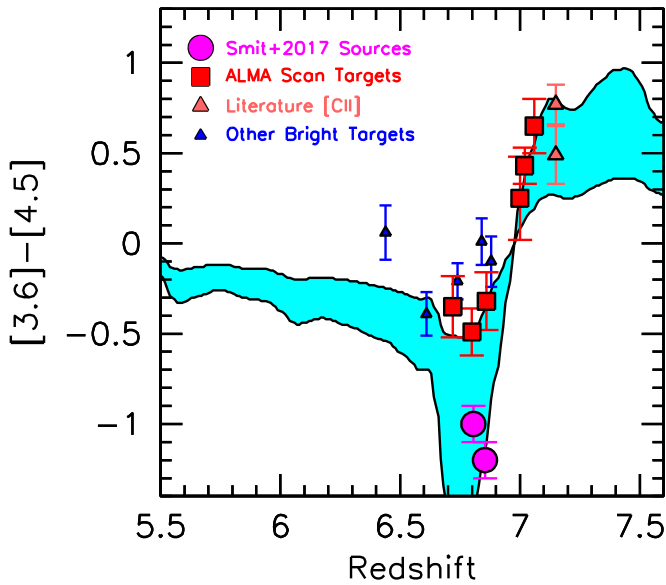


Figure 1. Measured [3.6]–[4.5] colors for the bright $z \sim 7$ galaxy candidates we have identified within UltraVISTA. The [3.6]–[4.5] color is largely driven by how high the EWs of the emission lines ([O III]+H β , H α) that fall in the [3.6] and [4.5] bands are, with the blue colors at $z \sim 6.6$ – 6.9 driven by the [O III]+H β lines falling in the [3.6] band, and at $z > 7$ the [O III]+H β lines falling in the [4.5] band. The most promising $z \sim 7$ follow-up targets are indicated by the red squares and correspond to the brightest $H \lesssim 25$ mag sources over COSMOS and show red or blue [3.6]–[4.5] colors, significantly narrowing the width of the redshift likelihood distribution over which [C II] searches are required. The filled magenta circles show the [3.6]–[4.5] colors measured for the two $z \sim 7$ galaxies with [C II] detections reported in Smit et al. (2018), while the solid orange triangles are for sources with [C II] detections in the literature (Pentericci et al. 2016; Matthee et al. 2017; Hashimoto et al. 2019). The blue triangles correspond to those bright ($H \leq 24.5$ mag) $z \sim 7$ galaxies from the Appendix, where the redshift is less well constrained based on the [3.6]–[4.5] colors (UVISTA-Z-002, 003, 004, 005, 008). The cyan shaded region shows the expected [3.6]–[4.5] colors for star-forming galaxies vs. redshift assuming a rest-frame equivalent width for [O III]+H β in the range 400–2000 Å.

colors. One particularly interesting opportunity exists for sources where the broadband Lyman-break places sources around a redshift $z \sim 7$, as Smit et al. (2015) and Smit et al. (2018) have already demonstrated. This is due to the fact that, at $z \sim 7$, the Spitzer/IRAC color can reduce the width of the redshift likelihood window for a source by as much as a factor of 2. Due to the dramatic impact the [O III]+H β lines have on the [3.6]–[4.5] colors for star-forming galaxies at $z \sim 7$, the Spitzer/IRAC color places robust constraints on the redshift of a source. For sources with a robustly red Spitzer/IRAC [3.6]–[4.5] color, we can eliminate the $z < 7$ solution, while for sources with a robustly blue Spitzer/IRAC [3.6]–[4.5] color, we can eliminate the $z > 7$ solution.

Following from these arguments, the best targets for the detection of luminous [C II] line emission at $z > 6$ are those sources (1) that are bright ($H < 25$), (2) have photometric Lyman breaks around $z \sim 7$, and (3) have robustly red or blue colors ($|[3.6] - [4.5]| - 1\sigma > 0.0$). We highlight these sources in a Spitzer/IRAC [3.6]–[4.5] color versus redshift diagram in Figure 1 as the large red squares.

The [O III]+H β equivalent widths derived from the IRAC colors of our selected sources are shown in Section 3.1. Because of the color requirement, the average EW of our sources (1155 Å) is significantly higher than the median EW (759 $^{+112}_{-113}$ Å) of the population of luminous $z \sim 7$ derived by Endsley et al. (2021).

It should be noted that red rest-frame optical colors could also be driven by strong Balmer breaks resulting from the presence of older stellar populations (Hashimoto et al. 2018; Roberts-Borsani et al. 2020; Strait et al. 2020). However, the presence of a possible Balmer break (rest-frame 3646 Å) starts impacting the observed IRAC color from $z \gtrsim 7.6$ after it moves into the 3.6 μ m channel. Because our galaxies have photometric redshifts below this, we will assume that observed IRAC colors are driven by [O III]+H β emission.

2.4. ALMA Observations and Data Reduction

A summary of the ALMA data collected for this second pilot program is presented in Table 1. ALMA observations were obtained over a contiguous 10.75 GHz range (two tunings) to scan for [C II] line. For the three targets with photometric redshifts $z \lesssim 7$, the redshift range $z = 6.57$ – 6.91 was scanned (240.28–251.02 GHz). For the targets with photometric redshifts $z \gtrsim 7$, the redshift range $z = 6.94$ – 7.31 was scanned (228.62–239.37 GHz). This observing setup utilizing the same scan windows for multiple targets was chosen to enable a significant reduction in calibration overheads from ALMA by targeting multiple sources in the same science goal. The scan windows utilized are presented in Figure 2, along with the redshift likelihood distribution inferred from our photometry. These scan windows cover between 71% to 99% of the estimated redshift likelihood distribution (Table 1). The required integration times for the observations were set assuming a similar [C II] luminosity and line width for sources as in pilot program observations of Smit et al. (2018), i.e., $\sim 4 \times 10^8 L_{\odot}$ and 200 km s $^{-1}$ for the FWHM of [C II]. To detect this line at $>5\sigma$, we required achieving a sensitivity of 300 μ Jy per 66 km s $^{-1}$ channel. To achieve this sensitivity, we require ~ 33 – 39 minutes of integration time with ALMA.

The ALMA data were reduced and calibrated using CASA version 5.4.1 following the standard ALMA pipeline procedures. To reduce the data size of the visibility measurement set, we averaged the data in bins of 30 s after carefully calculating that this bin size does not impact our data through time-average smearing (e.g., Thompson et al. 2017). We then performed initial imaging of the full data cube using the TCLEAN task with natural weighting. We clean to a depth of 3σ per channel and use automasking¹¹ to identify regions that contain emission. This initial data cube was used to do an initial search for [C II] line candidates; details of our line search procedure are described in the next section.

If a significant emission-line candidate is identified, we use the line properties to carefully mask the channels containing line emission to produce a continuum subtracted visibility data set using the UVCONTSUB task. This continuum subtracted measurement set is then used to reimage the full data cube, after which we repeat the line search and verify that the same line candidates are obtained.

For each emission-line candidate, we produce an initial moment-zero image, including channels that fall within $2 \times$ the initial FWHM estimate of the line candidate.¹² Using this moment-zero map, we produce a 1D spectrum where we

¹¹ For the automasking, we use the recommended settings for the 12 meter array with compact baselines from the CASA automasking guide: https://casaguides.nrao.edu/index.php/Automasking_Guide. We verified that the automasking identifies the same emission regions that we would have selected when masking by hand.

¹² Collapsing over all channels that fall within $2 \times$ the FWHM captures $\sim 98\%$ of the flux for lines with a Gaussian line profile.

Table 1
Main Parameters of the ALMA Observations Used for This Study

Source Name	R.A.	Decl.	Beamwidth ^a (arcsec)	Integration Time ^b (min.)	PWV (mm)	Frequency/Redshift Range of the Spectral Scan Percentage of $p(z)$ ^d (GHz)
UVISTA-Z-001	10:00:43.36	02:37:51.3	$1''.47 \times 1.21$	39.31	3.3	228.62–239.37 ($z = 6.94$ – 7.31) (71%)
UVISTA-Z-007	09:58:46.21	02:28:45.8	$1''.40 \times 1''.19$	32.76	1.9	240.28–251.02 ($z = 6.57$ – 6.91) (82%)
UVISTA-Z-009	10:01:52.30	02:25:42.3	$1''.38 \times 1''.20$	32.76	1.9	240.28–251.02 ($z = 6.57$ – 6.91) (65%)
UVISTA-Z-010	10:00:28.12	01:47:54.5	$1''.44 \times 1''.18$	39.31	3.3	228.62–239.37 ($z = 6.94$ – 7.31) (90%)
UVISTA-Z-013	09:59:19.35	02:46:41.3	$1''.45 \times 1''.18$	39.31	3.3	228.62–239.37 ($z = 6.94$ – 7.31) (99%)
UVISTA-Z-019	10:00:29.89	01:46:46.4	$1''.39 \times 1''.18$	32.76	1.9	240.28–251.02 ($z = 6.57$ – 6.91) (95%)

Notes.

^a Beam size for the naturally weighted moment-zero images.

^b Corresponds to the average on-source integration time for the two tunings.

^c Average precipitable water vapor during the observations.

^d Percentage of the redshift probability distribution that is covered by the spectral scan.

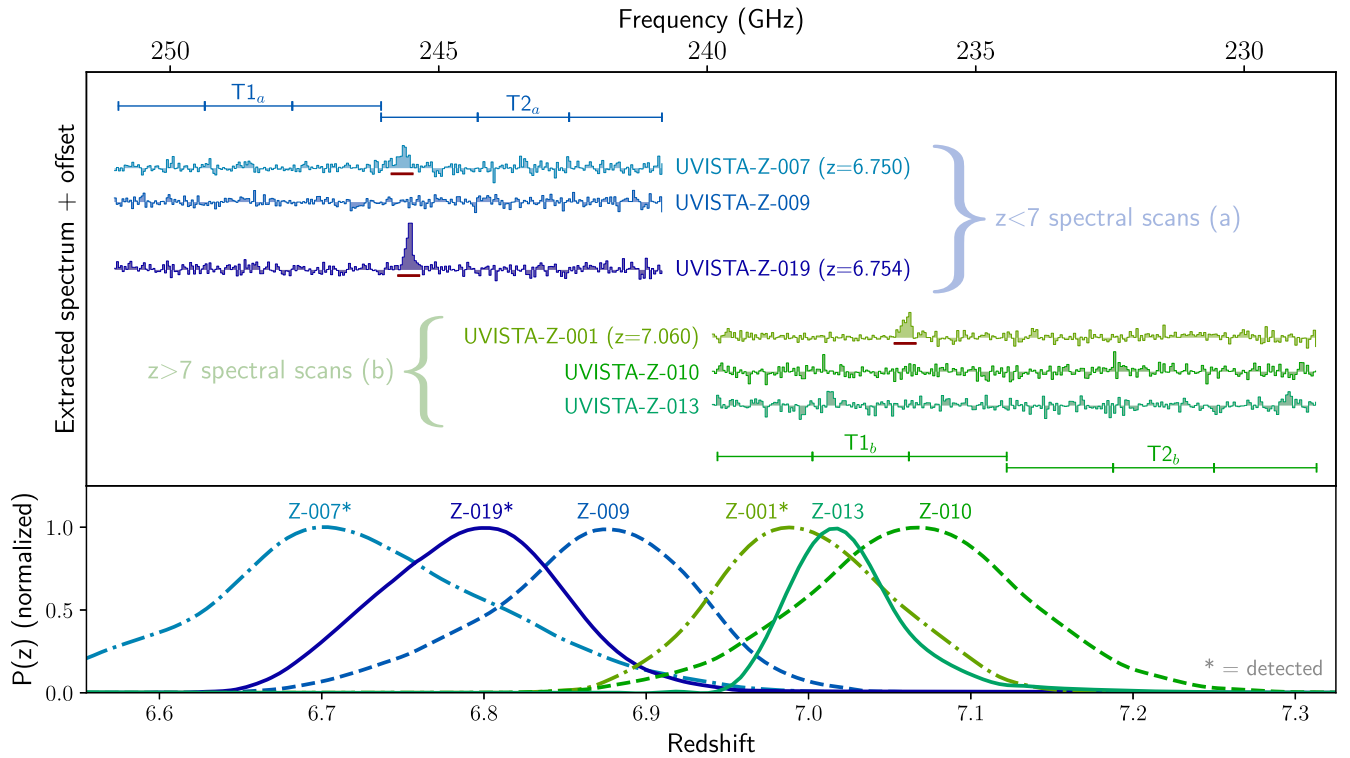


Figure 2. (Top) Full spectral scans as observed for the six galaxies targeted in this study. The targets are divided in two samples of three galaxies, which were observed with different ALMA tunings. For both samples, the ALMA tunings are shown above or below the spectral scans. We detect an emission line for three targets, indicated with a red line below the location of the emission line in the scans. For clarity, the spectra are binned combining five spectral channels. (Bottom) Photometric redshift probability distributions for the galaxies targeted in this study (on the same scale as the spectral scans). Galaxies for which an emission line is detected are indicated with asterisks. The two samples with different ALMA tunings are distinguished with blue and green colors.

include all pixel spectra that correspond to $>3\sigma$ emission in the moment-zero map and we weigh the contribution of each pixel-spectrum by its signal-to-noise level. We then fit a Gaussian line model to this spectrum in order to extract the central frequency and the FWHM. Next, using this updated estimate for the FWHM, we update the moment-zero image and its associated signal-to-noise weighted 1D spectrum. We perform this 10 times and note that it converges to a stable solution within a few iterations. The line parameters that we derive with this method are also used to carefully exclude line emission from the continuum imaging used in Schouws et al. (2022).

3. Results

3.1. [C II] Line Search

We performed a systematic search for emission-line candidates using the MF3D line search algorithm (Pavesi et al. 2018). MF3D finds line candidates using Gaussian template matching, which accounts for both spectrally and spatially extended emission lines. We used MF3D with 10 frequency templates with line widths ranging from 50 to 600 km s⁻¹ and 10 spatial templates ranging from 0'' to 4''5. To be considered a reliable detection, we require line candidates to be within 1''5 of the rest-frame UV position of our sources and have $S/N > 5.2\sigma$. This criterion was found to result in $>95\%$ purity (S. Schouws et al. 2023, in preparation).¹³

We require this high purity because our sources lack a prior spectroscopic redshift. A correct determination of the spectroscopic redshift is of particular importance for potential follow-up studies looking at other emission lines, which would be misguided if the spectroscopic redshift turns out to be incorrect. This strict signal-to-noise limit, however, comes at the cost of completeness, missing potential lines that are (just) below the detection limit.

Based on this search, we find reliable emission lines for UVISTA-Z-001 at 12.8σ at 235.80 GHz, for UVISTA-Z-007 at 9.4σ at 245.24 GHz, and for UVISTA-Z-019 at 18.3σ at 245.12 GHz. The other data cubes did not contain any line candidates that meet the S/N requirements discussed above. For these nondetections, it is possible that their [C II] luminosity falls below our detection limit ($\sim 2 \times 10^8 L_{\odot}$; see Section 4) or their redshift falls outside of the range scanned in this study. The results of the line search are summarized in Figure 2, which shows the layout of the full spectral scan and corresponding $P(z)$ values for all six sources in this study.

For the sources that are not detected in this study, we note that UVISTA-Z-009 has been detected just outside the scan range presented in this paper at $z = 6.984$ in the REBELS survey (Bouwens et al. 2022; S. Schouws et al. 2023, in preparation). The remaining two nondetections (UVISTA-Z-010 and UVISTA-Z-013) are the sources with the highest [O III]+H β equivalent widths (see Table 2). Their high [O III]+H β EWs indicate that these galaxies have a high ionization parameter, which could reduce the abundance of singly ionized carbon to more highly ionized states (e.g., Ferrara et al. 2019). However, studies of [C II] emission from dwarf galaxies in the local Universe show that the covering fraction of PDRs and the

¹³ With a 95% purity, we mean that for every 20 detected lines above the S/N threshold, at most one of the line candidates is actually a random noise feature. This threshold is directly derived from the noise statistics of the observed data cubes by comparing the occurrence of negative and positive features at different S/N values (e.g., Béthermin et al. 2020).

Table 2
Results—UV and ALMA Derived Properties of the Galaxies Targeted in This Study

Source Name	z_{phot}	z_{spec}	L_{UV}^{a} (arcsec)	$\log M_{*}^{\text{a}} M_{\odot}$	EW O III+H β^{b} (Å)	L_{IR}^{c} $10^{11} L_{\odot}$	$S_{\nu} \Delta \nu$ (Jy km s $^{-1}$)	$L_{[\text{C II}]} 10^8 L_{\odot}$	FWHM $^{\text{d}}$ (km s $^{-1}$)
UVISTA-Z-001	$7.00^{+0.05}_{-0.06}$	7.0599(3)	$2.9^{+0.1}_{-0.1}$	$9.58^{+0.09}_{-0.35}$	1004^{+442}_{-206}	$5.0^{+2.1}_{-2.1}$	0.57 ± 0.08	6.7 ± 1.2	256 ± 27
UVISTA-Z-007	$6.72^{+0.10}_{-0.09}$	6.7496(5)	$1.5^{+0.2}_{-0.2}$	$9.57^{+0.35}_{-0.44}$	761^{+530}_{-168}	$< 2.2^{\text{e}}$	0.51 ± 0.09	5.6 ± 1.4	301 ± 42
UVISTA-Z-009	$6.86^{+0.07}_{-0.06}$...	$1.6^{+0.2}_{-0.2}$	$9.40^{+0.32}_{-0.29}$	1012^{+677}_{-257}	< 2.4	...	$< 1.6^{\text{f}}$...
UVISTA-Z-010	$7.06^{+0.07}_{-0.07}$...	$1.1^{+0.2}_{-0.2}$	$8.88^{+0.28}_{-0.09}$	1706^{+780}_{-807}	< 2.1	...	$< 1.7^{\text{f}}$...
UVISTA-Z-013	$7.02^{+0.03}_{-0.03}$...	$1.4^{+0.4}_{-0.3}$	$10.72^{+0.03}_{-0.10}$	1821^{+4364}_{-1142}	< 2.2	...	$< 1.9^{\text{f}}$...
UVISTA-Z-019	$6.80^{+0.05}_{-0.06}$	6.7534(2)	$1.0^{+0.1}_{-0.1}$	$9.51^{+0.19}_{-0.18}$	628^{+226}_{-99}	$2.7^{+0.9}_{-0.9}$	0.80 ± 0.06	8.8 ± 0.9	184 ± 15

Notes.

^a UV luminosities and stellar masses are taken from Schouws et al. (2022) and were derived using the methodology described in Stefanon et al. (2019), assuming a metallicity of $0.2 Z_{\odot}$, a constant star formation history, and a Calzetti et al. (2000) dust law.

^b [O III]+H β equivalent widths are taken from Bouwens et al. (2022) and Stefanon et al. (2023, in preparation).

^c Total infrared luminosity integrated from 8 to 1000 μm assuming a modified blackbody SED with a dust temperature of 50 K and a dust emissivity index $\beta_{\text{dust}} = 1.6$, after correcting for CMB effects (we refer to Schouws et al. 2022 for details).

^d Observed FWHM of the [C II] emission line as measured in the 1D spectrum.

^e UVISTA-Z-007 shows dust continuum emission at a level of 2.5σ (corresponding to $L_{\text{IR}} \sim 1.8 \times 10^{11} L_{\odot}$), but we use the 3σ upper limit on the luminosity for the remainder of our analysis, to be conservative.

^f These nondetections are either caused by a [C II] luminosity below our detection limit or because their redshift falls outside of the range scanned in this study (see Table 1). Denoted is the average limiting luminosity over the scanned redshift range ($< 5.2\sigma$, assuming 350 km s $^{-1}$ FWHM).

^g The limiting luminosity scales with the square root of FWHM, i.e., broader lines are more difficult to detect. We have verified that the assumed FWHM does not significantly impact the results presented in this paper.), but atmospheric absorption can increase this limiting luminosity by a factor $\sim 2\times$; see Section 4.

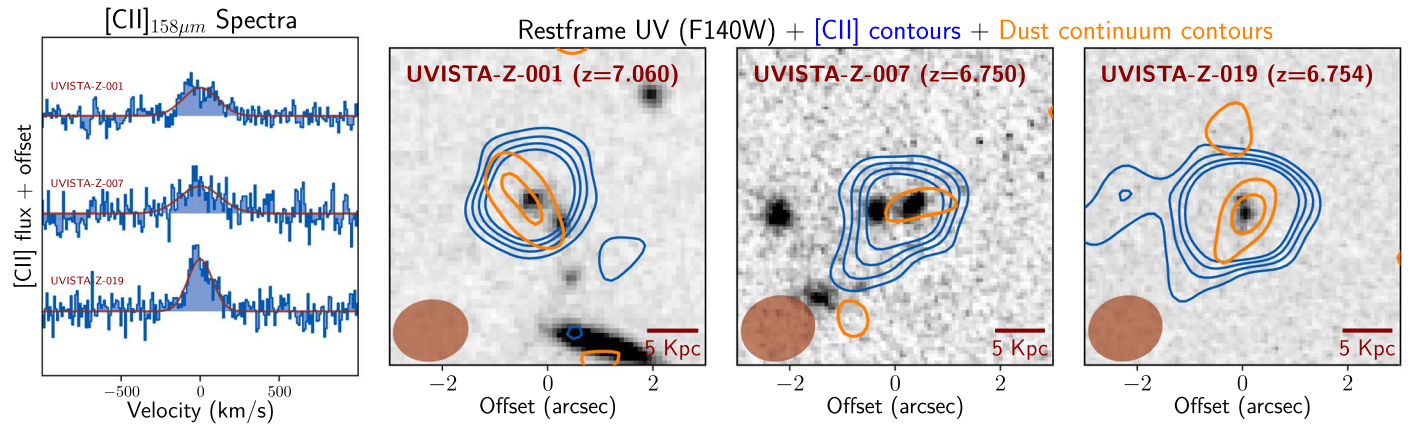


Figure 3. Overview of the galaxies detected in [C II] in this study. (left panel) 1D extracted spectra of the [C II] line (blue) and a Gaussian fit (red) for UVISTA-Z-001 (top), UVISTA-Z-007 (middle), and UVISTA-Z-019 (bottom). (right panels) The spatial distribution of the [C II] line emission (blue contours) relative to rest-UV images of the sources from HST (F140W: background image) and dust continuum emission (orange contours). Contours correspond to 2, 3, 4, and $5 \times$ the noise level. The dust continuum is significantly detected in UVISTA-Z-001 and UVISTA-Z-019 and marginally detected in UVISTA-Z-007 (at 2.5σ) (see also Schouws et al. 2022, for an extensive discussion of the continuum properties of these galaxies).

fraction of [C II] emission from neutral regions increases with ionization parameter (Cormier et al. 2019). Further studies are necessary to explore this for the objects presented in this paper.

For the detected sources, we show the contours from the [C II] and dust continuum emission compared to the rest-frame UV morphology and their 1D spectra in Figure 3. The rest-frame UV images are in the F140W band at $1.39 \mu\text{m}$ and are from GO-13793 (UVISTA-Z-001, PI: Bowler; Bowler et al. 2017) and GO-16506 (UVISTA-Z-007, UVISTA-Z-019, PI: Witstok; Witstok et al. 2022). For a detailed description of the procedure we used to produce the moment-zero images and 1D spectra, we refer to Section 2.4. For the nondetections, only ground-based rest-frame UV imaging is available (available in Figure 12 in Schouws et al. (2022) or Figure A1 in Inami et al. (2022).

We measure the integrated flux of the [C II] emission lines from the moment-zero images by fitting the data with a one-component Gaussian model using the IMFIT task. The resulting flux measurements are shown in Table 2. We double-check the measurements from IMFIT with UVMULTIFIT (Martí-Vidal et al. 2014), which we use to fit a Gaussian model in the (u, v) plane instead of the image plane. We find that, reassuringly, both methods produce results consistent within their error bars. Finally, we convert these [C II] fluxes to luminosities following Solomon et al. (1992) and Carilli et al. (2013):

$$L_{[\text{C II}]} / L_{\odot} = 1.04 \times S_{\nu} \Delta\nu \times \nu_{\text{obs}} \times D_L^2, \quad (1)$$

where $S_{\nu} \Delta\nu$ is the integrated flux density in mJy km s^{-1} , ν_{obs} is the observing frequency, and D_L is the luminosity distance.

3.2. The [C II]–SFR Relation

The large luminosity and favorable atmospheric opacity of [C II] enable detection up to very high redshifts. Local galaxies studies have found a tight correlation between the [C II] luminosity and SFR (De Looze et al. 2011, 2014; Kapala et al. 2014; Cormier et al. 2015; Herrera-Camus et al. 2015; Díaz-Santos et al. 2017), and [C II] has therefore been proposed as an efficient and unbiased probe of the SFR at high redshift.

In past few years, this correlation between SFR and $L_{[\text{C II}]}$ has been observed out to $z \sim 8$ with an increasing number of detections and upper limits. Of particular note are the results

from the ALPINE large program, which finds little-to-no evolution in the [C II]–SFR relation in a large sample of normal galaxies at $4.4 < z < 5.9$ (Schaerer et al. 2020). At even higher redshifts, the current samples are less uniform, but they still seem to be consistent with the local relation, albeit with a larger scatter (e.g., Carniani et al. 2018; Matthee et al. 2019).

Nevertheless, there has been an increasing number of observations of galaxies that fall well below the local relations (e.g., Ota et al. 2014; Laporte et al. 2019; Matthee et al. 2019; Bakx et al. 2020; Binggeli et al. 2021; Jolly et al. 2021; Rybak et al. 2021; Uzgil et al. 2021). Currently, it is not clear what is the driver of this deficit in [C II] luminosity for some high-redshift galaxies.

We show the position of our sources on the [C II]–SFR relation in Figure 4, and find that the galaxies targeted in this study are also consistent with the local relation from De Looze et al. (2014) within the expected scatter. The three sources where [C II] remains undetected are not shown on this figure, because it is unclear whether the [C II] line is below our detection threshold (i.e., $L_{[\text{C II}]} < 2 \times 10^8 L_{\odot}$) or whether the true redshift is outside the range of our spectral scan. Because these sources have SFRs between 15 and $25 M_{\odot} \text{ yr}^{-1}$, our detection limit falls within the scatter of the local relation (De Looze et al. (2014)). From this figure, it is clear that most of the $z > 6.5$ galaxies with $\text{SFR} \gtrsim 20 M_{\odot} \text{ yr}^{-1}$ are consistent with the local relation, while at lower SFRs a significant fraction of currently observed galaxies seem to fall below the relation.

3.3. [C II] versus FIR

It has been found that [C II] can account for up to $\sim 1\%$ of the total infrared luminosity of galaxies; however, it has also been found that this fraction decreases by ~ 2 orders of magnitude with increasing L_{IR} , leading to a [C II] deficit in luminous galaxies (e.g., Genzel & Cesarsky 2000; Malhotra et al. 2001; Hodge & da Cunha 2020). Specifically, observed [C II]/FIR ratios range from $\sim 10^{-2}$ for normal $z \sim 0$ galaxies to $\sim 10^{-4}$ for the most luminous objects, with a large scatter (e.g., Díaz-Santos et al. 2013).

The reason for this observed [C II] deficit remains a topic of discussion in the literature, with a large range of possible explanations, including optically thick [C II] emission, effects from AGN, changes in the IMF, thermal saturation of [C II],

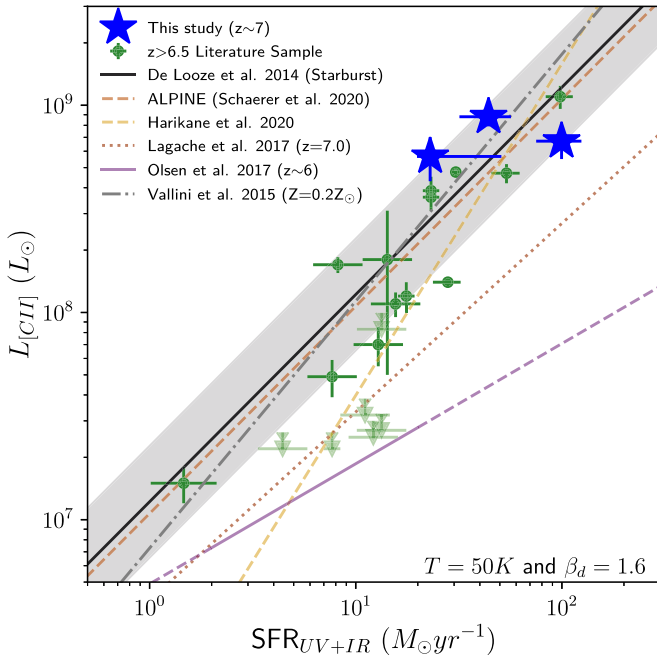


Figure 4. [C II]–SFR relation for the galaxies in this study (solid blue stars). Our results are consistent with the results from De Looze et al. (2014) for local H II/Starburst galaxies within the scatter (solid black line and gray shaded region). For context, we show results from previous $z > 6.5$ detections and nondetections (from the compilation by Matthee et al. 2019) (green data points and upper limits). We also show some fits to the $L_{\text{[C II]}}$ –SFR relation from the literature for observations (Harikane et al. 2020; Schaerer et al. 2020), semi-analytic models (Lagache et al. 2018, at $z = 7$), and zoom-in simulations by Olsen et al. (2017) and Vallini et al. (2015) (with $Z = 0.2Z_{\odot}$). All SFRs have been scaled to a Chabrier IMF (Chabrier 2003), and IR luminosities are calculated assuming a modified blackbody curve with $T = 50\text{K}$ and $\beta_d = 1.6$ (as described in Schouws et al. 2022).

positive dust grain charging, and dust-dominated H II region opacities (e.g., Casey et al. 2014; Smith et al. 2016; Ferrara et al. 2019; Rybak et al. 2019; Hodge & da Cunha 2020).

The galaxies in this study have far-infrared luminosities of $L_{\text{IR}} = 1\text{--}5 \times 10^{11} L_{\odot}$,¹⁴ placing them in the Luminous Infrared Galaxy (LIRG) classification. Comparing their infrared to their [C II] luminosity, we find ratios of $[\text{C II}]/L_{\text{IR}} \sim 1\text{--}3 \times 10^{-3}$ (see Figure 5). Compared to local (U)LIRGS from the GOALS survey (Díaz-Santos et al. 2013, 2017), we find that our galaxies are less deficient in [C II] by a factor ~ 0.3 dex. This result has a minor dependence on the assumed dust temperature, as shown with the gray arrows on Figure 5. When assuming higher or lower dust temperatures, the data points move mostly parallel to the trend. Only for substantially higher dust temperatures ($\gtrsim 70\text{ K}$) would our measurements be consistent with the local results.

Our measured [C II]/FIR ratios are consistent with other studies at high redshifts, which also find that high-redshift galaxies tend to be less [C II] deficient (e.g., Capak et al. 2015; Schaerer et al. 2020). A possible explanation for this lack of [C II] deficit in high-redshift galaxies could be different dust conditions. Specifically, a lower dust-to-gas ratio at a fixed far-infrared luminosity could increase the [C II] luminosity with respect to the infrared (Capak et al. 2015).

¹⁴ To calculate the far-infrared luminosities, we assume a modified blackbody dust SED with $T = 50\text{ K}$ and $\beta = 1.6$; see Schouws et al. (2022) for details.

3.4. [C II] Kinematics

Due to its high intrinsic luminosity, [C II] is an efficient tracer of the kinematics of high-redshift galaxies (e.g., Neeleman et al. 2019). To investigate the kinematics of our sources, we derive the velocity maps of our galaxies by fitting Gaussians to the pixel spectra in our cube, including all pixels for which the uncertainty on the velocity is less than 50 km s^{-1} . The resulting velocity fields are shown in Figure 6. Despite the low ($\sim 1''.3$; see Table 1) resolution of our observations, some of our sources show significant velocity gradients.

In particular, we find that both UVISTA-Z-001 and UVISTA-Z-007 display a significant velocity gradient, with velocity amplitudes of $v_{\text{amp}} \sin(i) = 108^{+45}_{-36}\text{ km s}^{-1}$ and $v_{\text{amp}} \sin(i) = 119^{+87}_{-50}\text{ km s}^{-1}$, respectively.¹⁵ If we compare the observed rotational velocities assuming no correction for inclination ($i = 0$, hence $v_{\text{obs}} = v_{\text{amp}} \sin(i)$) to the total line width of the 1D spectrum (σ_{obs}) (see Table 2 and Figure 6), we find that the $v_{\text{obs}}/\sigma_{\text{obs}}$ are $1.0^{+0.6}_{-0.4}$ and $0.9^{+0.9}_{-0.5}$, respectively. This would mean that both sources should most likely be classified as rotation dominated (defined as $v_{\text{obs}}/\sigma_{\text{obs}} > 0.8$ as utilized in, e.g., Förster-Schreiber et al. 2009). This calculation does not assume a correction for the inclination of the system, which would increase $v_{\text{obs}}/\sigma_{\text{obs}}$. The observed velocity gradient could, however, also be caused by close mergers. At the current resolution, rotating disks are indistinguishable from mergers (e.g., Jones et al. 2021, S. Schouws et al. 2023, in preparation).

In particular, we find indications that UVISTA-Z-007 could be a merger. The HST F140W imaging (J. Witstok et al. 2023, in preparation) shows clearly that this source consists of two distinct components (see Figure 3). The observed velocity gradient is in the same direction as the two UV components (as shown in Figure 6), making it likely that the observed velocity gradient in the [C II] is in fact due to the merger of these two components.

The HST F140W imaging of UVISTA-Z-001 also consists of two components with consistent photometric redshifts (Bowler et al. 2017). However, for this source, the observed velocity gradient is perpendicular to the direction of the two components. Moreover, it seems that the [C II] emission as well as the dust continuum emission primarily originate from the northernmost component. This is despite the similarity of their rest-frame UV properties (Bowler et al. 2017). The reason for this discrepancy between the FIR properties of both components will require more detailed observations.

For UVISTA-Z-019, we do not observe a significant velocity gradient, and we constrain the maximum rotation velocity to $v_{\text{amp}} \sin(i) < 50\text{ km s}^{-1}$, implying that this system is either dominated by dispersion or a face-on system ($i = 0$). A more detailed look at the pixel spectra within the cube indicates that, in the central part of this source, the [C II] emission seems to break down into two distinct components (rightmost panel on Figure 6), consisting of a narrow component (FWHM $\sim 70\text{ km s}^{-1}$) responsible for $\sim 20\%$ of the total flux and a broad component (FWHM $\sim 220\text{ km s}^{-1}$) that accounts for $\sim 80\%$ of the total flux.

This interesting spectral feature could be caused by several processes, such as the effect of an outflow. However, this

¹⁵ We derive $v_{\text{amp}} \sin(i)$ by fitting a rotating thin disk model to the 3D data cube using forward modeling with our kinematics fitting code SKITTER (S. Schouws et al. 2023, in preparation). The maximum velocities on the kinematics maps shown in Figure 6 are lower than the actual $v_{\text{amp}} \sin(i)$, due to beam-smearing effects.

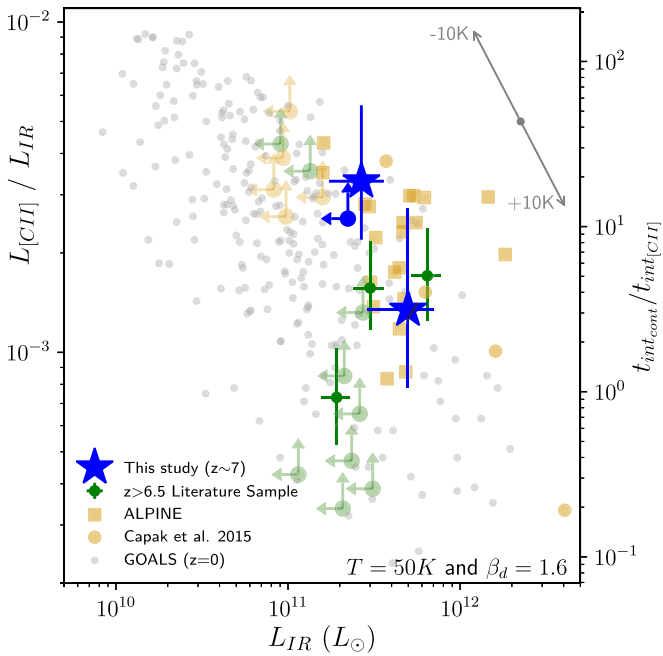


Figure 5. Ratio of the observed [C II] luminosity $L_{[\text{C II}]}$ to the IR luminosity L_{IR} as a function of L_{IR} for our small $z \sim 7$ galaxy sample (solid blue stars, 1σ uncertainties). IR luminosities L_{IR} are estimated assuming a modified blackbody SED with dust temperature 50K and an emissivity index β_d of 1.6. With the gray arrows in the top right corner, we show the effect of changing the assumed dust temperature by $\pm 10\text{K}$. For context, we also show results from the $z = 0$ GOALS sample (Díaz-Santos et al. 2013, 2017, gray circles), the $z \sim 4\text{--}6$ ALPINE sample (Béthermin et al. 2020; Faisst et al. 2020; Le Fèvre et al. 2020, yellow squares), and other results from the literature (green circles). Lower limits on $L_{[\text{C II}]} / L_{\text{IR}}$ and upper limits on L_{IR} are 3σ . On the right vertical axis, the ratio of integration times required to detect [C II]₁₅₈ at 5σ to the time required to detect sources in the dust continuum at 3σ is indicated. Our new measurements show slightly higher $L_{[\text{C II}]} / L_{\text{IR}}$ ratios than the $z = 0$ GOALS results at a given L_{IR} , and they appear to be qualitatively very similar to the $z \sim 4\text{--}6$ results obtained by ALPINE.

would imply that the majority of the [C II] luminosity originates from the outflow and that the emission from the galaxy would have a very narrow FWHM, implying a low dynamical mass that is lower than the stellar mass ($M_{\text{dyn}} \sim 9 \times 10^8 M_\odot$ ¹⁶ versus $M_* \sim 3 \times 10^9 M_\odot$). An alternative explanation for the spectral feature could be a minor merger, where the narrow component originates from an infalling galaxy. However, this would mean that the LOS velocity is rather small at only $\Delta V \sim 50 \text{ km s}^{-1}$, despite this likely being one of the final stages of the merger. Indeed, HST morphology tentatively shows two close components separated by $\sim 1.5 \text{ kpc}$ (see also Figure 3). Finally, the kinematics could also be evidence for a bright clump of intense star formation within a larger system, indicating the complex structure of high-redshift sources (e.g., Kohandel et al. 2019, 2020). Hence, an alternative interpretation of the clumps in HST imaging could be the presence of multiple star-forming regions in a larger system. Higher spatial resolution ALMA observations or deep rest-frame optical observations with JWST would be invaluable to definitively distinguish between these scenarios.

¹⁶ We derive dynamical masses following Wang et al. (2013): $\frac{M_{\text{dyn}}}{M_\odot \sin(i)} = 1.94 \times 10^5 \cdot \left(\frac{\text{FWHM}}{\text{km s}^{-1}}\right)^2 \cdot \frac{r_{1/2}}{\text{kpc}}$, where FWHM is the full width at half maximum of the [C II] line in km s^{-1} and $r_{1/2}$ the [C II] half-light radius in kpc. Because the narrow [C II] component is unresolved, we assume a size of $r_{1/2} \sim 1 \text{ kpc}$ (consistent with Bowler et al. 2017).

4. The Efficiency of Spectral Scans and Future Prospects

In this study, we have obtained redshifts for three galaxies without a prior spectroscopic redshift. In particular by targeting UV-luminous galaxies with high SFRs, the [C II] lines we detect are also luminous. In Figure 7, we show that the [C II] emission of our sources could have been detected at $>5\sigma$ in only ~ 20 minute integrations per tuning with ALMA.¹⁷

Our sources benefit from very tight constraints on the photometric redshift, due to the large break in the IRAC colors (see Figure 1), which enables us to cover a significant fraction of the $P(z)$ with only two tunings. For sources that lack this additional constraint, three or four tunings would be necessary to cover the $P(z)$ appropriately. Nevertheless, this would still mean that galaxies like the ones targeted in this study could be spectroscopically confirmed in less than $<1.5 \text{ hr}$ per source.

It should be noted though that, for sources with a lower SFR (and hence lower [C II] luminosities), spectral scanning quickly becomes expensive. A spectral scan targeting an L_* galaxy ($\text{SFR}_{\text{UV}} \sim 8 M_\odot \text{ yr}^{-1}$ at $z = 7$) would cost $\sim 12 \text{ hr}$ on source adopting the De Looze et al. (2014) $L_{[\text{C II}]} \text{--SFR}$ relation. Therefore, to study the [C II] emission from $L \leq L_*$ galaxies, either targeting lensed galaxies for spectral scans or following up galaxies with a prior spectroscopic redshift (e.g., from JWST or ground-based Ly α) remain the most suitable options.

One significant advantage of using a spectral scan strategy is the time spent integrating in regions of the spectra not containing prominent ISM cooling lines. These integrations allow us to probe continuum emission from our targets. This is important because the continuum is much harder to detect than [C II], as one can see from the [C II]/ L_{IR} ratios of our sources. This is illustrated in Figure 5 (right vertical axis), on which we show the ratio of the integration time needed to detect the dust continuum versus the [C II] line. We find that it is necessary to integrate up to $\sim 20\times$ longer to obtain a 3σ detection of the dust continuum. This means that the time spent observing tunings that do not contain a spectral line is not wasted, but rather contributes to the necessary sensitivity to detect the faint dust continuum.

Based on the results presented in this paper and Smit et al. (2018), we proposed and were awarded the time to apply the spectral scan method to a significantly larger sample of galaxies, covering a much larger range in galaxy properties and redshift. The result was the ongoing Reionization Era Bright Emission Line Survey (REBELS) large program, in which we pursue spectral scans for [C II] or [O III] in a sample of 40 $z > 6.5$ galaxies (Bouwens et al. 2022).

5. Summary

In this paper, we present the results of new ALMA spectral scan observations targeting [C II] in a small sample of six luminous Lyman-break galaxies at $z \sim 7$. The targeted sources were identified from deep, wide-area near-IR, optical, and Spitzer/IRAC observations and are particularly luminous. The targeted sources also feature tight constraints on their redshifts, leveraging the abrupt changes that occur in the IRAC color around $z \sim 7$ (where strong line emission from [O III]+H β shifts from the [3.6] to [4.5] band). This improves the

¹⁷ Based on the ALMA sensitivity calculator: <https://almascience.eso.org/proposing/sensitivity-calculator> and the ALMA Cycle 8 Technical Handbook: <https://almascience.nrao.edu/documents-and-tools/cycle8/alma-technical-handbook>

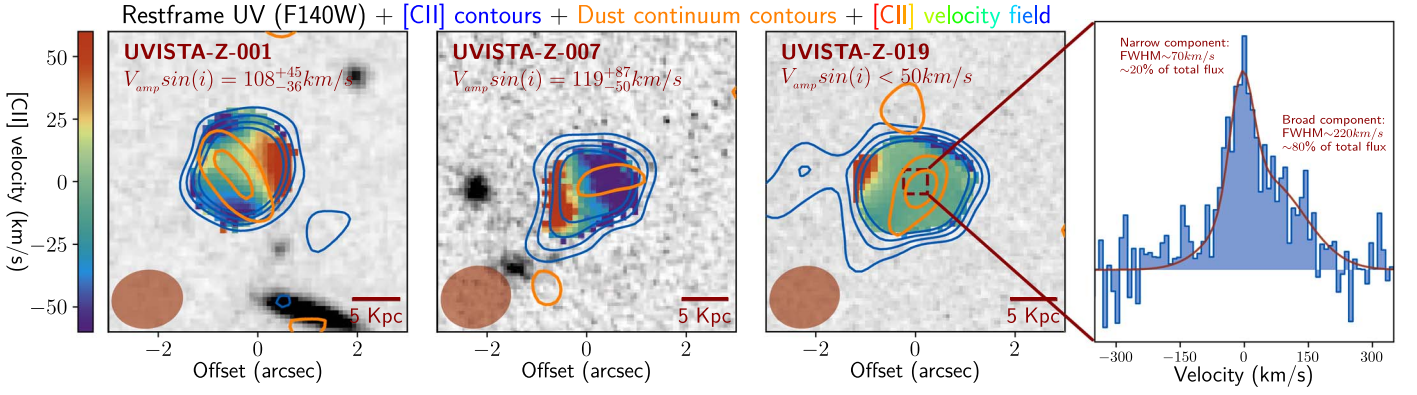


Figure 6. (left three panels) Low-resolution [C II] kinematics of our sources overlaid on the rest-UV imaging with the [C II] and dust continuum contours, as in Figure 3. The velocity gradients for all sources are shown on the same scale, from -60 km s^{-1} (blue) to 60 km s^{-1} (red). (rightmost panel) Zoom-in on the central pixel spectra of UVISTA-Z-019. The spectrum consists of a narrow component (FWHM $\sim 70 \text{ km s}^{-1}$) responsible for $\sim 20\%$ of the total flux and a broad component (FWHM $\sim 220 \text{ km s}^{-1}$) that accounts for $\sim 80\%$ of the total flux.

efficiency of the spectral scans by $\sim 2 \times$, based on the small number of tunings required to cover the inferred $P(z)$. The present results build on the exciting results from Smit et al. (2018), who previously demonstrated the potential of spectral scans for [C II] with just two sources.

Our main results are summarized below:

1. We detect ($>9\sigma$) [C II] lines for three of the six galaxies we target with our spectral scans (shown in Figure 2). The [C II] lines are strong with luminosities between $5.6 \times 10^8 L_\odot$ and $8.8 \times 10^8 L_\odot$. We also observe that the [C II], dust, and rest-frame UV emission are well aligned within the resolution of our observation (see Figure 3).
2. Placing our new detections on the [C II]–SFR relation shows that our sources are consistent with the local relation from De Looze et al. (2014) (for H II/starburst galaxies, as shown in Figure 4), and we find slightly higher $[\text{C II}]/L_{\text{IR}} \sim 1\text{--}3 \times 10^{-3}$ compared to local (U) LIRGS (see Figure 5), which is consistent with previous studies of high-redshift galaxies.
3. Although our observations are taken at a relatively low resolution ($\sim 1''3$), we find that our sources display a broad spectrum of kinematic diversity. One of our sources seems to be rotation dominated, one source is most likely a major merger, and one source is dominated by dispersion. We also find possible kinematic evidence for a bright star-forming clump within the dispersion-dominated source (see Figure 6). However, higher-resolution observations are necessary to confirm our interpretation of the kinematics of our sources.
4. We discuss the lack of evolution of the [C II]–SFR relation found for luminous high-redshift galaxies by reviewing the literature on the physical effects that drive the [C II] emission in high-redshift galaxies. While one would naively expect a trend toward lower [C II]/SFR values with redshift based on the higher ionization parameter, lower metallicities, and higher densities of high-redshift galaxies, this is not observed. We speculate that a lower dust-to-gas or dust-to-metal ratio, which increases the [C II] emission, could compensate for those effects.

These new results illustrate the tremendous potential spectral scans with ALMA have for characterizing luminous galaxies in the epoch of reionization (see Figure 7), including deriving

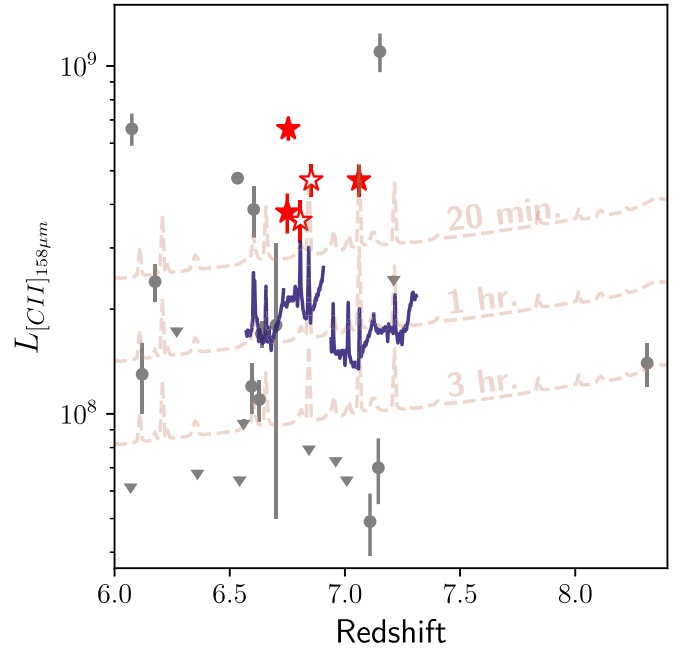


Figure 7. In this study, we have presented a method to identify and efficiently spectroscopically confirm the redshifts of luminous [C II] emitting galaxies (solid (this study) and open (Smit et al. 2018) red stars). We compare the derived luminosities of our sources to the literature (gray data points and upper limits). The present compilation is from Matthee et al. (2019) and Bakx et al. (2020). The newly discovered lines are more luminous than most previous detections. The luminosities of those sources without [C II] detections are less clear, but for those sources where our scans cover the full likelihood distribution, it is likely that the lines are fainter and more in line with the typical sources. For context, we show the expected limiting luminosities (for a 5.2σ detection and 350 km s^{-1} FWHM) that can be achieved with ALMA with 20, 60, and 180 minute integrations (red dashed lines) and find that our targets could have been detected in as little as 20 minutes per scan window. We also indicate the achieved depth of our observations (30–40 minutes) with the solid blue lines. This demonstrates the great potential to use ALMA for spectral scans to obtain spectroscopic redshifts of UV-luminous galaxies in the epoch of reionization.

spectroscopic redshifts for sources, and probing the kinematics and dynamical masses of sources, as well as the dust continuum (Schouws et al. 2022). Results from this data set showed the potential (Section 4) and were important in successfully proposing for the REBELS large program in cycle 7 (Bouwens et al. 2022). Future studies (S. Schouws et al. 2023, in

preparation) will significantly add to the current science using that considerable data set.

Acknowledgments

We are greatly appreciative to our ALMA program coordinator Daniel Harsono for support with our ALMA program. This paper makes use of the following ALMA data: ADS/JAO.ALMA 2018.1.00085.S. ALMA is a partnership of ESO (representing its member states), NSF (USA) and NINS (Japan), together with NRC (Canada), MOST and ASIAA (Taiwan), and KASI (Republic of Korea), in cooperation with the Republic of Chile. The Joint ALMA Observatory is operated by ESO, AUI/NRAO and NAOJ. Sander Schouws and Rychard Bouwens acknowledge support from TOP grant TOP1.16.057 and a NOVA (Nederlandse Onderzoekschool Voor Astronomie) 5 grant. J.H. acknowledges support of the VIDI research program with project number 639.042.611,

which is (partly) financed by the Netherlands Organisation for Scientific Research (NWO). H.S.B.A. acknowledges support from the NAOJ ALMA Scientific Research Grant Code 2021-19A. J.W. and R.S. acknowledge support from the ERC Advanced Grant 695671, “QUENCH,” and the Fondation MERAC. R.S. acknowledges support from an STFC Ernest Rutherford Fellowship (ST/S004831/1). The P.I. acknowledges assistance from Allegro, the European ALMA Regional Center node in the Netherlands.

Appendix

Bright Sample of $z \sim 7$ Galaxies Used for Selecting Our Six Follow-up Targets

For completeness, we provide the coordinates, magnitudes, [3.6]–[4.5] colors, and photometric redshifts for the full selection of bright $z \sim 7$ candidate galaxies we identified (Section 2.2) within the UltraVISTA field in Table 3.

Table 3
Candidate $z \sim 7$ Galaxies in the UltraVISTA DR3 Observations

ID	R.A.	Decl.	m_{AB}^a	[3.6]–[4.5]	z_{phot}^b	z_{spec}	References ^c
Current Selection of Bright Candidate $z \sim 7$ Galaxies							
UVISTA-Z-001	10:00:43.361	2:37:51.33	23.8 ± 0.1	0.3 ± 0.2	$7.00^{+0.05}_{-0.06}$	7.060^g	[2]
UVISTA-Z-002 ^e	10:02:06.469	2:13:24.18	24.1 ± 0.1	-0.2 ± 0.1	$6.74^{+0.06}_{-0.06}$		[1,10]
UVISTA-Z-003 ^e	10:02:06.701	2:34:21.42	24.2 ± 0.1	-0.1 ± 0.1	$6.88^{+0.08}_{-0.08}$		
UVISTA-Z-004 ^e	10:01:36.850	2:37:49.10	24.3 ± 0.1	0.0 ± 0.1	$6.84^{+0.09}_{-0.09}$		[2,10]
UVISTA-Z-005 ^e	10:01:58.501	2:33:08.22	24.3 ± 0.1	-0.4 ± 0.1	$6.61^{+0.10}_{-0.10}$		[1,10]
UVISTA-Z-006	10:01:40.688	1:54:52.37	24.4 ± 0.1	0.5 ± 0.2	$7.09^{+0.06}_{-0.05}$	7.152^g	[2,9]
UVISTA-Z-007	09:58:46.214	2:28:45.75	24.4 ± 0.1	-0.4 ± 0.2	$6.72^{+0.10}_{-0.09}$	7.750^f	
UVISTA-Z-008	09:58:39.762	2:15:03.27	24.4 ± 0.1	0.1 ± 0.2	$6.44^{+0.05}_{-0.05}$		
UVISTA-Z-009 ^e	10:01:52.304	2:25:42.27	24.5 ± 0.1	-0.3 ± 0.2	$6.86^{+0.07}_{-0.06}$		[2]
UVISTA-Z-010	10:00:28.121	1:47:54.47	24.5 ± 0.1	0.6 ± 0.2	$7.06^{+0.07}_{-0.07}$		[2]
UVISTA-Z-011 ^e	10:00:42.125	2:01:57.10	24.6 ± 0.1	-0.1 ± 0.1	$6.55^{+0.05}_{-0.06}$		[2,10]
UVISTA-Z-013 ^e	09:59:19.353	2:46:41.31	24.8 ± 0.2	0.4 ± 0.1	$7.02^{+0.03}_{-0.03}$		[10]
UVISTA-Z-014	09:57:35.723	1:44:56.40	24.8 ± 0.1	$-^d$	$7.13^{+0.15}_{-0.16}$		
UVISTA-Z-015	10:00:23.772	2:20:36.98	24.8 ± 0.1	0.8 ± 0.1	$7.07^{+0.03}_{-0.03}$	7.154^h	[2,3,4,5,6,7]
UVISTA-Z-016	10:01:54.562	2:47:35.79	24.9 ± 0.2	-1.1 ± 0.9	$6.77^{+0.24}_{-0.26}$		
UVISTA-Z-017	10:00:30.188	2:15:59.71	24.9 ± 0.1	-1.3 ± 0.2	$6.78^{+0.04}_{-0.04}$	6.854^i	[1,2,3,4,8,10]
UVISTA-Z-018 ^e	10:02:03.811	2:13:25.06	25.0 ± 0.2	-0.6 ± 0.3	$6.81^{+0.12}_{-0.10}$		[2]
UVISTA-Z-019	10:00:29.892	1:46:46.37	25.0 ± 0.2	-0.5 ± 0.1	$6.80^{+0.05}_{-0.06}$	7.753^f	
UVISTA-Z-020	10:01:57.140	2:33:48.76	25.0 ± 0.2	-0.6 ± 0.3	$6.73^{+0.12}_{-0.11}$		
UVISTA-Z-021	09:57:36.994	2:05:11.28	25.1 ± 0.2	-0.3 ± 0.3	$6.73^{+0.16}_{-0.16}$		[10]
UVISTA-Z-022	09:59:13.206	2:21:52.51	25.1 ± 0.2	-0.1 ± 0.6	$6.52^{+0.14}_{-0.16}$		
UVISTA-Z-023	09:58:45.961	2:39:05.94	25.1 ± 0.2	-3.4 ± 7.3	$6.76^{+0.13}_{-0.13}$		
UVISTA-Z-024	09:59:04.558	2:11:38.10	25.2 ± 0.2	-0.8 ± 0.4	$6.89^{+0.15}_{-0.14}$		
UVISTA-Z-025	09:58:49.216	1:39:09.70	25.3 ± 0.3	-1.6 ± 0.6	$6.70^{+0.12}_{-0.12}$		[10]
UVISTA-Z-026	10:02:05.967	2:06:46.13	25.3 ± 0.2	-1.4 ± 0.4	$6.74^{+0.06}_{-0.06}$		[10]
UVISTA-Z-027	09:59:22.426	2:31:19.45	25.3 ± 0.2	0.1 ± 0.7	$6.69^{+0.11}_{-0.11}$		[10]
UVISTA-Z-028	10:00:54.819	1:50:05.28	25.3 ± 0.2	-0.1 ± 0.2	$6.67^{+0.18}_{-0.16}$		[10]
UVISTA-Z-029	10:00:41.097	2:29:31.13	25.3 ± 0.2	-0.1 ± 0.1	$6.72^{+0.16}_{-0.17}$		
UVISTA-Z-030	10:02:22.458	2:04:45.72	25.3 ± 0.3	-0.1 ± 0.2	$6.61^{+0.11}_{-0.10}$		
UVISTA-Z-031	09:59:01.407	2:28:02.13	25.4 ± 0.2	-0.9 ± 0.4	$6.61^{+0.19}_{-0.23}$		
UVISTA-Z-032	10:00:22.482	1:45:32.62	25.4 ± 0.2	-1.0 ± 0.4	$6.71^{+0.11}_{-0.17}$		

Notes.

^a UVISTA H -band magnitude.

^b 68% confidence intervals derived by EAZY using the SED template set presented in Section 2.2.

^c References: (1) Tilvi et al. 2013; (2) Bowler et al. 2014, 2017; (3) Bouwens et al. 2015; (4) Smit et al. 2015; (5) Roberts-Borsani et al. 2016; (6) Pentericci et al. 2016; (7) Stark et al. 2017; (8) Smit et al. 2018; (9) Hashimoto et al. 2019; (10) Endsley et al. 2021.

^d This source fell outside the footprint of the IRAC mosaics used for the source selection in this manuscript.

^e These sources are targeted in the REBELS program (Bouwens et al. 2022).















^f This paper (ADS/JAO.ALMA 2018.1.00085.S).

^g Detected in dust continuum, [C II] and [O III] by Hashimoto et al. (2019) (ADS/JAO.ALMA 2016.1.00954.S) and dust continuum by Bowler et al. (2018) (ADS/JAO.ALMA 2015.1.00540.S) (Big Three Dragons/ B14-65666).

^h Detected in [C II] by Pentericci et al. (2016) (ADS/JAO.ALMA 2015.1.01105.S) and $Ly\alpha$ by Stark et al. (2017).

ⁱ Detected in [C II] by Smit et al. (2018) (ADS/JAO.ALMA 2015.1.01111.S).

ORCID iDs

Sander Schouws  <https://orcid.org/0000-0001-9746-0924>
 Rychard Bouwens  <https://orcid.org/0000-0002-4989-2471>
 Renske Smit  <https://orcid.org/0000-0001-8034-7802>
 Jacqueline Hodge  <https://orcid.org/0000-0001-6586-8845>
 Mauro Stefanon  <https://orcid.org/0000-0001-7768-5309>
 Joris Witstok  <https://orcid.org/0000-0002-7595-121X>
 Juliette Hilhorst  <https://orcid.org/0000-0000-0000-0000>
 Ivo Labbé  <https://orcid.org/0000-0002-2057-5376>
 Hiddo Algera  <https://orcid.org/0000-0002-4205-9567>
 Leindert Boogaard  <https://orcid.org/0000-0002-3952-8588>
 Michael Maseda  <https://orcid.org/0000-0003-0695-4414>
 Pascal Oesch  <https://orcid.org/0000-0001-5851-6649>
 Huub Röttgering  <https://orcid.org/0000-0001-8887-2257>
 Paul van der Werf  <https://orcid.org/0000-0001-5434-5942>

References

- Ashby, M. L. N., Willner, S. P., Fazio, G. G., et al. 2013, *ApJ*, **769**, 80
 Anders, P., & Fritze-v. A. U. 2003, *A&A*, **401**, 1063
 Ashby, M. L. N., Caputi, K. I., Cowley, W., et al. 2018, *ApJS*, **237**, 39
 Ashby, M. L. N., Willner, S. P., Fazio, G. G., et al. 2015, *ApJS*, **218**, 33
 Atek, H., Siana, B., Scarlata, C., et al. 2011, *ApJ*, **743**, 121
 Bakx, T. J. L. C., Tamura, Y., Hashimoto, T., et al. 2020, *MNRAS*, **493**, 4294
 Bertin, E., & Arnouts, S. 1996, *A&AS*, **117**, 393
 Béthermin, M., Fudamoto, Y., Ginolfi, M., et al. 2020, *A&A*, **643**, A2
 Binggeli, C., Inoue, A. K., Hashimoto, T., et al. 2021, *A&A*, **646**, A26
 Bouwens, R. J., Illingworth, G. D., Oesch, P. A., et al. 2015, *ApJ*, **803**, 34
 Bouwens, R. J., Oesch, P. A., Stefanon, M., et al. 2021, *AJ*, **162**, 47
 Bouwens, R. J., Smit, R., Schouws, S., et al. 2022, *ApJ*, **931**, 160
 Bowler, R. A. A., Bourne, N., Dunlop, J. S., McLure, R. J., & McLeod, D. J. 2018, *MNRAS*, **481**, 1631
 Bowler, R. A. A., Cullen, F., McLure, R. J., Dunlop, J. S., & Avison, A. 2022, *MNRAS*, **510**, 5088
 Bowler, R. A. A., Dunlop, J. S., McLure, R. J., et al. 2014, *MNRAS*, **440**, 2810
 Bowler, R. A. A., Dunlop, J. S., McLure, R. J., & McLeod, D. J. 2017, *MNRAS*, **466**, 3612
 Bradač, M., Garcia-Appadoo, D., Huang, K.-H., et al. 2017, *ApJL*, **836**, L2
 Brammer, G. B., van Dokkum, P. G., & Coppi, P. 2008, *ApJ*, **686**, 1503
 Burgasser, A. J., McElwain, M. W., Kirkpatrick, J. D., et al. 2004, *AJ*, **127**, 2856
 Calzetti, D., Armus, L., Bohlin, R. C., et al. 2000, *ApJ*, **533**, 682
 Capak, P. L., Carilli, C., Jones, G., et al. 2015, *Natur*, **522**, 455
 Carilli, C. L., Riechers, D., Walter, F., et al. 2013, *ApJ*, **763**, 120
 Carniani, S., Ferrara, A., Maiolino, R., et al. 2020, *MNRAS*, **499**, 5136
 Carniani, S., Maiolino, R., Smit, R., & Amorín, R. 2018, *ApJL*, **854**, L7
 Casey, C. M., Narayanan, D., & Cooray, A. 2014, *PhR*, **541**, 45
 Chabrier, G. 2003, *PASP*, **115**, 763
 Cormier, D., Abel, N. P., Hony, S., et al. 2019, *A&A*, **626**, A23
 Cormier, D., Madden, S. C., Lebouteiller, V., et al. 2015, *A&A*, **578**, A53
 De Looze, I., Baes, M., Bendo, G. J., Cortese, L., & Fritz, J. 2011, *MNRAS*, **416**, 2712
 De Looze, I., Cormier, D., Lebouteiller, V., et al. 2014, *A&A*, **568**, A62
 Díaz-Santos, T., Armus, L., Charmandaris, V., et al. 2013, *ApJ*, **774**, 68
 Díaz-Santos, T., Armus, L., Charmandaris, V., et al. 2017, *ApJ*, **846**, 32
 Endsley, R., Stark, D. P., Chevallard, J., & Charlot, S. 2021, *MNRAS*, **500**, 5229
 Erben, T., Hildebrandt, H., Lerchster, M., et al. 2009, *A&A*, **493**, 1197
 Faist, A. L., Fudamoto, Y., Oesch, P. A., et al. 2020, *MNRAS*, **498**, 4192
 Fazio, G. G., Hora, J. L., Allen, L. E., et al. 2004, *ApJS*, **154**, 10
 Ferrara, A., Vallini, L., Pallottini, A., et al. 2019, *MNRAS*, **489**, 1
 Finkelstein, S. L., Papovich, C., Dickinson, M., Song, M., et al. 2013, *Natur*, **502**, 524
 Finkelstein, S. L., Ryan, R. E., Papovich, C., et al. 2015, *ApJ*, **810**, 71
 Förster-Schreiber, N. M., Genzel, R., Bouché, N., et al. 2009, *ApJ*, **706**, 1364
 Fudamoto, Y., Oesch, P., Faist, A., et al. 2020, *A&A*, **643**, A4
 Fudamoto, Y., Oesch, P. A., Schouws, S., et al. 2021, *Natur*, **597**, 489
 Galametz, A., Grazian, A., Fontana, A., et al. 2013, *ApJS*, **206**, 10
 Genzel, R., & Cesarsky, C. J. 2000, *ARA&A*, **38**, 761
 Guo, Y., Ferguson, H. C., Giallisco, M., et al. 2013, *ApJS*, **207**, 24
 Harikane, Y., Ono, Y., Ouchi, M., et al. 2022, *ApJS*, **259**, 20
 Harikane, Y., Ouchi, M., Inoue, A. K., et al. 2020, *ApJ*, **896**, 93
 Harikane, Y., Ouchi, M., Shibuya, T., et al. 2018, *ApJ*, **859**, 84
 Hashimoto, T., Inoue, A. K., Mawatari, K., et al. 2019, *PASJ*, **71**, 71
 Hashimoto, T., Laporte, N., Mawatari, K., et al. 2018, *Natur*, **557**, 392
 Herrera-Camus, R., Bolatto, A. D., Wolfire, M. G., et al. 2015, *ApJ*, **800**, 1
 Hodge, J. A., & da Cunha, E. 2020, *RSOS*, **7**, 200556
 Inami, H., Algera, H. S. B., Schouws, S., et al. 2022, *MNRAS*, **515**, 3126
 Ishigaki, M., Kawamata, R., Ouchi, M., et al. 2018, *ApJ*, **854**, 73
 Jolly, J.-B., Knudsen, K., Laporte, N., et al. 2021, *A&A*, **652**, A128
 Jones, G. C., Vergani, D., Romano, M., et al. 2021, *MNRAS*, **507**, 3540
 Kapala, M. J., Sandstrom, K., Groves, B., et al. 2014, *ApJ*, **798**, 24
 Kirkpatrick, J. D., Cushing, M. C., Gelino, C. R., et al. 2011, *ApJS*, **197**, 19
 Knudsen, K. K., Richard, J., Kneib, J.-P., et al. 2016, *MNRAS Lett.*, **462**, L6
 Kohandel, M., Pallottini, A., Ferrara, A., et al. 2019, *MNRAS*, **487**, 3007
 Kohandel, M., Pallottini, A., Ferrara, A., et al. 2020, *MNRAS*, **499**, 1250
 Kotulla, R., Fritze, U., Weibacher, P., & Anders, P. 2009, *MNRAS*, **396**, 462
 Kron, R. G. 1980, *ApJS*, **43**, 305
 Labbé, I., Bouwens, R., Illingworth, G. D., & Franx, M. 2006, *ApJL*, **649**, L67
 Labbé, I., González, V., Bouwens, R. J., et al. 2010a, *ApJL*, **708**, L26
 Labbé, I., González, V., Bouwens, R. J., et al. 2010b, *ApJL*, **716**, L103
 Labbé, I., Oesch, P. A., Bouwens, R. J., et al. 2013, *ApJL*, **777**, L19
 Labbé, I., Oesch, P. A., Illingworth, G. D., et al. 2015, *ApJ*, **803**, 221, 23
 Lagache, G., Cousin, M., & Chatzikos, M. 2018, *A&A*, **609**, A130
 Laporte, N., Katz, H., Ellis, R. S., et al. 2019, *MNRAS Lett.*, **487**, L81
 Le Fèvre, O., Béthermin, M., Faist, A., et al. 2020, *A&A*, **643**, A1
 Malhotra, S., Kaufman, M. J., Hollenbach, D., et al. 2001, *ApJ*, **561**, 766
 Martí-Vidal, I., Vlemmings, W. H. T., Muller, S., & Casey, S. 2014, *A&A*, **563**, A136
 Matthee, J., Sobral, D., Boogaard, L. A., et al. 2019, *ApJ*, **881**, 124
 Matthee, J., Sobral, D., Boone, F., et al. 2017, *ApJ*, **851**, 145
 McCracken, H. J., Milvang-Jensen, B., Dunlop, J., et al. 2012, *A&A*, **544**, A156
 McLure, R. J., Dunlop, J. S., Bowler, R. A. A., et al. 2013, *MNRAS*, **432**, 2696
 Neeleman, M., Bañados, E., Walter, F., et al. 2019, *ApJ*, **882**, 10
 Oesch, P. A., Bouwens, R. J., Illingworth, G. D., et al. 2015, *ApJ*, **808**, 104
 Oke, J. B., & Gunn, J. E. 1983, *ApJ*, **266**, 713
 Olsen, K., Greve, T. R., Narayanan, D., et al. 2017, *ApJ*, **846**, 105
 Ono, Y., Ouchi, M., Mobasher, B., et al. 2012, *ApJ*, **744**, 83
 Ota, K., Walter, F., Ohta, K., et al. 2014, *ApJ*, **792**, 34
 Patten, B. M., Stauffer, J. R., Burrows, A., et al. 2006, *ApJ*, **651**, 502
 Pavesi, R., Sharon, C. E., Riechers, D. A., et al. 2018, *ApJ*, **864**, 49
 Pentericci, L., Carniani, S., Castellano, M., et al. 2016, *ApJL*, **829**, L11
 Riechers, D. A., Carilli, C. L., Capak, P. L., et al. 2014, *ApJ*, **796**, 84
 Roberts-Borsani, G. W., Bouwens, R. J., Oesch, P. A., et al. 2016, *ApJ*, **823**, 143
 Roberts-Borsani, G. W., Ellis, R. S., & Laporte, N. 2020, *MNRAS*, **497**, 3440
 Robertson, B. E. 2022, *ARA&A*, **60**, 121
 Rybak, M., da Cunha, E., Groves, B., et al. 2021, *ApJ*, **909**, 130
 Rybak, M., Rivera, G. C., Hodge, J. A., et al. 2019, *ApJ*, **876**, 112
 Sanders, D. B., Salvato, M., Aussel, H., et al. 2007, *ApJS*, **172**, 86
 Schaerer, D., & de Barros, S. 2009, *A&A*, **502**, 423
 Schaerer, D., Ginolfi, M., Béthermin, M., et al. 2020, *A&A*, **643**, A3
 Schouws, S., Stefanon, M., Bouwens, R., et al. 2022, *ApJ*, **928**, 31
 Scoville, N., Aussel, H., Brusa, M., et al. 2007, *ApJS*, **172**, 1
 Skelton, R. E., Whitaker, K. E., Momcheva, I. G., et al. 2014, *ApJS*, **214**, 24
 Smit, R., Bouwens, R. J., Carniani, S., et al. 2018, *Natur*, **553**, 178
 Smit, R., Bouwens, R. J., Franx, M., et al. 2015, *ApJ*, **801**, 122
 Smith, J. D. T., Croxall, K., Draine, B., et al. 2016, *ApJ*, **834**, 5
 Solomon, P. M., Downes, D., & Radford, S. J. E. 1992, *ApJL*, **387**, L55
 Stark, D. P., Ellis, R. S., Charlot, S., et al. 2017, *MNRAS*, **464**, 469
 Stark, D. P., Ellis, R. S., Chiu, K., Ouchi, M., & Bunker, A. 2010, *MNRAS*, **408**, 1628
 Stefanon, M., Bouwens, R. J., Labbé, I., et al. 2022, *ApJ*, **927**, 48
 Stefanon, M., Labbé, I., Bouwens, R. J., et al. 2019, *ApJ*, **883**, 99
 Stefanon, M., Yan, H., Mobasher, B., et al. 2017, *ApJS*, **229**, 32
 Strait, V., Bradac, M., Coe, D., et al. 2020, *ApJ*, **888**, 124
 Szalay, A. S., Connolly, A. J., & Szokoly, G. P. 1999, *AJ*, **117**, 68
 Taniguchi, Y., Scoville, N., Murayama, T., et al. 2007, *ApJS*, **172**, 9
 Tilvi, V., Papovich, C., Tran, K. V. H., et al. 2013, *ApJ*, **768**, 56
 Thompson, A. R., Moran, J. M., & Swenson, Jr., G. W. 2017, *Interferometry and Synthesis in Radio Astronomy* (3rd ed.; Berlin: Springer)
 Uzgil, B. D., Oesch, P. A., Walter, F., et al. 2021, *ApJ*, **912**, 67
 Vallini, L., Gallerani, S., Ferrara, A., Pallottini, A., & Yue, B. 2015, *ApJ*, **813**, 36
 van der Wel, A., Straughn, A. N., Rix, H. W., et al. 2011, *ApJ*, **742**, 111
 Venemans, B. P., Walter, F., Neeleman, M., et al. 2020, *ApJ*, **904**, 130
 Wagg, J., Carilli, C. L., Wilner, D. J., et al. 2010, *A&A*, **519**, L1
 Walter, F., Riechers, D., Cox, P., et al. 2009, *Natur*, **457**, 699
 Wang, R., Wagg, J., Carilli, C. L., et al. 2013, *ApJ*, **773**, 44
 Weaver, J. R., Kauffmann, O. B., Ilbert, O., et al. 2022, *ApJS*, **258**, 11
 Willott, C. J., Carilli, C. L., Wagg, J., & Wang, R. 2015, *ApJ*, **807**, 180
 Witstok, J., Smit, R., Maiolino, R., et al. 2022, *MNRAS*, **515**, 1751
 Zittrn, A., Labbé, I., Belli, S., et al. 2015, *ApJL*, **810**, L12